IEEE Access
Multidisciplinary ⋮ Rapid Review ⋮ Open Access Journal

Received November 11, 2019, accepted November 25, 2019, date of publication December 3, 2019, date of current version March 10, 2020.

Digital Object Identifier 10.1109/ACCESS.2019.2957307

Multi-Channel SAR System Design for HRWS and GMTI in Low PRF

XUEPAN ZHANG[1], CHEN YANG[1], XUEJING ZHANG[2], (Student Member, IEEE), AND QINGQING LIN[1]

[1]Qian Xuesen Laboratory of Space Technology, China Academy of Space Technology, Beijing 100094, China
[2]University of Electronic Science and Technology of China, Chengdu 611731, China

Corresponding authors: Xuejing Zhang (xjzhang7@163.com) and Qingqing Lin (linqingqing@qxslab.cn)

This work was supported in part by the National Key Research and Development Program of China under Grant 2017YFB0503300 and Grant 2017YFB0503304, in part by the Youth Talent Promotion Project under Grant 17-JCJQ-QT-046, in part by the Joint Advance Research Program of Aerospace Science and Technology under Grant 6141B06160301, and in part by the National Natural Science Foundation of China (NSFC) under Grant 61701499, Grant 61773383, Grant 41604157, and Grant 11502278.

ABSTRACT High-resolution and wide-swath (HRWS) is an important challenge in synthetic aperture radar (SAR). Combined SAR with array, the azimuth dual-channel SAR configuration achieves high azimuth resolution and HRWS in low Pulse repetition frequency (PRF) by doppler band synthesizing technology. However, low PRF introduces ambiguity to ground moving target indication (GMTI). Interferometry is performed between two look data in the range frequency domain to resolve the ambiguity by decreasing the interferometry phase. As a result, the phase becomes insensitive to the radial velocity of moving targets. This condition brings difficultly in moving target detection. Two channels together with two equivalent channels are exploited fully to solve these problems. The four-channel interferometry is also conducted to improve the GMTI performance. Parameters, including system and motion parameters, are estimated unambiguously to complete HRWS imaging and GMTI. System parameter design is also considered to satisfy the requirements of HRWS and GMTI simultaneously. Simulations demonstrate the validity of the proposed methods.

INDEX TERMS HRWS, multichannel SAR, SAR-GMTI, low PRF, unambiguous parameters estimation.

I. INTRODUCTION

Synthetic aperture radar (SAR), which has high resolution, cloud penetrating property, and remote sensing capability, has been studied intensively in civil and military applications in recent years [1]–[6]. Simultaneous realization of high resolution and wide swath (HRWS), which is an important aspect of SAR image evaluation, is the goal of SAR researchers in pursuing efforts [7]–[10]. SAR combined with ground moving target indication (GMTI) (SAR–GMTI) has been designed to be an effective and convenient approach to realize moving target localization and recognition in the well-focused image domain [11], [12]. HRWS SAR–GMTI can realize GMTI in a considerably wide SAR scene, and this feature is beneficial for civilian and military applications. Thus, HRWS SAR–GMTI is strongly desirable.

SAR with wide observed swath can achieve HRWS SAR conveniently. However, the single-antenna SAR cannot achieve simultaneous HRWS SAR given the minimum antenna constraint [8], [13]. High azimuth resolution demands wide Doppler bandwidth. High pulse repetition frequency (PRF) is designed to avoid the Doppler spectrum ambiguity, whereas low PRF should be used for wide observed range swath to avoid the range ambiguity. The tradeoff between high and low PRF restricts the development of HRWS SAR. The array signal processing technique has been widely applied in radar, sonar, wireless communications and so on [14]–[24], which plays a much more important role in these fields. Based on the array architecture, the multichannel SAR systems offer great potential for HRWS imaging. Along track multichannel SAR with low PRF to achieve wide swath is used to suppress the Doppler ambiguity for realizing HRWS imaging [8]–[10].

Clutter suppression, which requires some spatial degrees of freedom in azimuth, should be performed in GMTI application to detect moving targets. The azimuth spatial degrees of freedom are also used for HRWS SAR to suppress the Doppler ambiguity; thus, HRWS SAR together with GMTI is

The associate editor coordinating the review of this manuscript and approving it for publication was Liangtian Wan.

difficult to realize when only several azimuth spatial degrees of freedom are available [8], especially for SAR. Existing moving target detection methods have some demands for PRF [7]. For example, the displaced phase center antenna (DPCA) method expects the PRF to meet the DPCA condition; the space–time adaptive processing method requires considerably higher PRF than the DPCA method [7]. However, low PRF is used in the HRWS SAR for wide swath, and this utilization causes difficulty in balancing the performance of HRWS and GMTI. Several authors have investigated and proposed useful methods to solve the problems in HRWS SAR–GMTI. In [8], the design of PRF is proposed to optimize the GMTI performance together with HRWS imaging. In [22], the optimum method is proposed using highly non-uniform PRF or ideally suited PRF for clutter suppression.

In the present study, the frequency band synthesizing technology, which has been used for range resolution improvement [25], [26], is utilized in the Doppler spectrum to improve the azimuth resolution. A slightly higher PRF than the Doppler bandwidth is intended to avoid the Doppler spectrum ambiguity and achieve wide observed swath. A dual-channel SAR with different Doppler centroids but the same Doppler bandwidth is synthesized to double the Doppler bandwidth, which enables low PRF to achieve high azimuth resolution and wide swath. Under this configuration of HRWS SAR, the GMTI is primarily analyzed. Interferometry between two look data in the range frequency domain is conducted to resolve the ambiguity estimation by decreasing the interferometry phase. Dual channels together with two equivalent channels are exploited fully to improve the GMTI performance.

The rest of the paper is structured as follows. In Section II, the signal model of dual channels together with two equivalent channels is provided. In Section III, Doppler band synthesizing technology is proposed to realize HRWS, and the basic GMTI is analyzed. In Section IV, the parameters are estimated for HRWS and GMTI, the ambiguity due to fast radial velocity of moving targets is presented, and two look-data interferometry methods are utilized to resolve the ambiguity. In Section V, a robust method, namely, four-channel interferometry, is proposed to solve the problem caused by the two look-data interferometry methods. In Section VI, the system parameter design is considered to satisfy the requirements of HRWS SAR–GMTI. In Section VII, simulations are conducted to demonstrate the effectiveness of the proposed methods.

II. SIGNAL MODELING

Dual-channel SAR is used as an example, and the proposed concept can be implemented in multichannel SAR. SAR of dual along track channels, with channel space of d, is adopted to realize HRWS. Channel 1 transmits linear frequency modulation (LFM) signal with carrier frequency of f_{c1}, and channel 2 transmits that with carrier frequency of f_{c2}. Channel isolation is analyzed in Section VI. The transmitted signals of

TABLE 1. Receiving patterns of dual channels.

Transmit channel	Receive channel	Signal expression
Channel 1	Channel 1	$s_1(\tau,\eta)$
Channel 2	Channel 2	$s_2(\tau,\eta)$
Channel 1	Channel 2	$s_3(\tau,\eta)$
Channel 2	Channel 1	$s_4(\tau,\eta)$

channels 1 and 2 can be written as

$$s_{t1}(\tau) = rect\left[\tau/T_r\right]\exp\left(j\pi f_{c1}\tau + j\pi K_r\tau^2\right), \quad (1)$$

$$s_{t2}(\tau) = rect\left[\tau/T_r\right]\exp\left(j\pi f_{c2}\tau + j\pi K_r\tau^2\right), \quad (2)$$

where τ is the fast time corresponding to the range dimension, K_r denotes the LFM ratio of the transmitted signal, T_r is the pulse width of the LFM signal, and the bandwidth B_r can be obtained by $B_r = K_rT_r$; $rect\,[x]$ denotes $|x| < 0.5$.

The stationary point target P in the center of the observed scene is analyzed. The instantaneous slant ranges from P to channels 1 and 2, namely, $R_1(\eta)$ and $R_2(\eta)$, can be expressed by the geometry relationship as

$$\begin{aligned} R_1(\eta) &= \sqrt{(R_n - v_{rel}\eta)^2 + (v\eta)^2} \\ &\approx R_n - v_{rel}\eta + \frac{(v\eta)^2}{2R_n}, \end{aligned} \quad (3)$$

$$\begin{aligned} R_2(\eta) &= \sqrt{(R_n - v_{rel}\eta)^2 + (v\eta - d)^2} \\ &\approx R_n - v_{rel}\eta + \frac{(v\eta - d)^2}{2R_n}, \end{aligned} \quad (4)$$

where v_{rel} is the relative radial velocity [13] between the SAR and the point target, and R_n denotes the nearest range from target P to the track. It should be noted that the azimuth velocity of the moving target is ignored here for simple, and the effect of the azimuth velocity would be analyzed in Section V. The approximation is obtained by using the Taylor expansion. The echoes of the transmitted signals by channels 1 and 2 can be obtained by the receiving patterns listed in TABLE 1, and the isolation among different echoes is analyzed in Section VI.

The received echoes can be given by

$$\begin{aligned} &s_{r1}(\tau,\eta) \\ &= \sigma_c rect\left[\frac{\tau - 2R_1(\eta)/c}{T_r}\right] rect\left[\frac{\eta}{T_a}\right] \\ &\quad\cdot \exp\left(j\pi f_{c1}\left(\tau - \frac{2R_1(\eta)}{c}\right) + j\pi K_r\left(\tau - \frac{2R_1(\eta)}{c}\right)^2\right), \end{aligned} \quad (5)$$

$$\begin{aligned} &s_{r2}(\tau,\eta) \\ &= \sigma_c rect\left[\frac{\tau - 2R_2(\eta)/c}{T_r}\right] rect\left[\frac{\eta}{T_a}\right] \\ &\quad\cdot \exp\left(j\pi f_{c2}\left(\tau - \frac{2R_2(\eta)}{c}\right) + j\pi K_r\left(\tau - \frac{2R_2(\eta)}{c}\right)^2\right), \end{aligned} \quad (6)$$

$$
\begin{aligned}
&s_{r3}(\tau,\eta)\\
&=\sigma_c rect\left[\frac{\tau-(R_1(\eta)+R_2(\eta))/c}{T_r}\right]rect\left[\frac{\eta}{T_a}\right]\\
&\quad\cdot\exp\left(j\pi f_{c1}\left(\tau-\frac{R_1(\eta)+R_2(\eta)}{c}\right)\right)\\
&\quad\cdot\exp\left(j\pi K_r\left(\tau-\frac{R_1(\eta)+R_2(\eta)}{c}\right)^2\right),
\end{aligned}
\tag{7}
$$

$$
\begin{aligned}
&s_{r4}(\tau,\eta)\\
&=\sigma_c rect\left[\frac{\tau-(R_1(\eta)+R_2(\eta))/c}{T_r}\right]rect\left[\frac{\eta}{T_a}\right]\\
&\quad\cdot\exp\left(j\pi f_{c2}\left(\tau-\frac{R_1(\eta)+R_2(\eta)}{c}\right)\right)\\
&\quad\cdot\exp\left(j\pi K_r\left(\tau-\frac{R_1(\eta)+R_2(\eta)}{c}\right)^2\right),
\end{aligned}
\tag{8}
$$

where σ_c denotes the complex reflection coefficient of the stationary point target and c is the speed of light.

To maintain $s_{r3}(\tau,\eta)$ and $s_{r4}(\tau,\eta)$ in the same form as $s_{r1}(\tau,\eta)$ and $s_{r2}(\tau,\eta)$, we let

$$
R_3(\eta)=R_4(\eta)=\frac{R_1(\eta)+R_2(\eta)}{2}. \tag{9}
$$

By using (3) and (4), (9) can be rewritten as

$$
R_3(\eta)=R_4(\eta)\approx R_n-v_{rel}\eta+\frac{(v\eta-d/2)^2}{2R_n}. \tag{10}
$$

$s_{r3}(\tau,\eta)$ and $s_{r4}(\tau,\eta)$ can be rewritten as

$$
\begin{aligned}
&s_{r3}(\tau,\eta)\\
&=\sigma_c rect\left[\frac{\tau-2R_3(\eta)/c}{T_r}\right]rect\left[\frac{\eta}{T_a}\right]\\
&\quad\cdot\exp\left(j\pi f_{c1}\left(\tau-\frac{2R_3(\eta)}{c}\right)+j\pi K_r\left(\tau-\frac{2R_3(\eta)}{c}\right)^2\right),
\end{aligned}
\tag{11}
$$

$$
\begin{aligned}
&s_{r4}(\tau,\eta)\\
&=\sigma_c rect\left[\frac{\tau-2R_4(\eta)/c}{T_r}\right]rect\left[\frac{\eta}{T_a}\right]\\
&\quad\cdot\exp\left(j\pi f_{c2}\left(\tau-\frac{2R_4(\eta)}{c}\right)+j\pi K_r\left(\tau-\frac{2R_4(\eta)}{c}\right)^2\right),
\end{aligned}
\tag{12}
$$

which are the equivalent channels 3 and 4 for convenience.

After range compression and migration correction, the received signals can be expressed as [8]

$$
\begin{aligned}
s_1(\tau,\eta)&=\sigma_c\sin c\left(B_r\left(\tau-\frac{2R_n}{c}\right)\right)rect\left[\frac{\eta}{T_a}\right]\\
&\quad\cdot\exp\left(-j\varphi_1+j2\pi f_{dc1}\eta-j\pi K_{a1}\eta^2\right),
\end{aligned}
\tag{13}
$$

$$
\begin{aligned}
s_2(\tau,\eta)&=\sigma_c\sin c\left(B_r\left(\tau-\frac{2R_n}{c}\right)\right)rect\left[\frac{\eta}{T_a}\right]\\
&\quad\cdot\exp\left(-j\varphi_2+j2\pi f_{dc2}\eta-j\pi K_{a2}\left(\eta-\frac{d}{v}\right)^2\right),
\end{aligned}
\tag{14}
$$

$$
\begin{aligned}
s_3(\tau,\eta)&=\sigma_c\sin c\left(B_r\left(\tau-\frac{2R_n}{c}\right)\right)rect\left[\frac{\eta}{T_a}\right]\\
&\quad\cdot\exp\left(-j\varphi_1+j2\pi f_{dc1}\eta-j\pi K_{a1}\left(\eta-\frac{d}{2v}\right)^2\right),
\end{aligned}
\tag{15}
$$

$$
\begin{aligned}
s_4(\tau,\eta)&=\sigma_c\sin c\left(B_r\left(\tau-\frac{2R_n}{c}\right)\right)rect\left[\frac{\eta}{T_a}\right]\\
&\quad\cdot\exp\left(-j\varphi_2+j2\pi f_{dc2}\eta-j\pi K_{a2}\left(\eta-\frac{d}{2v}\right)^2\right),
\end{aligned}
\tag{16}
$$

where the expressions of constant phase (φ_1 and φ_2), the Doppler centroid (f_{dc1} and f_{dc2}), and the Doppler chirp rate (K_{a1} and K_{a2}) can be written as

$$
\varphi_1=\frac{4\pi R_n f_{c1}}{c},\quad f_{dc1}=\frac{2v_{rel}f_{c1}}{c},\quad K_{a1}=\frac{2v^2f_{c1}}{cR_n}, \tag{17}
$$

$$
\varphi_2=\frac{4\pi R_n f_{c2}}{c},\quad f_{dc2}=\frac{2v_{rel}f_{c2}}{c},\quad K_{a2}=\frac{2v^2f_{c2}}{cR_n}. \tag{18}
$$

Notably, the signals of the four channels, which contain two equivalent channels (channel 3 $s_3(\tau,\eta)$ and channel 4 $s_4(\tau,\eta)$), possess different Doppler centroids and chirp rates. These properties enable HRWS imaging and GMTI, which are shown in the next section in detail.

III. PROPOSED METHODS

We exploit the same and different properties of different channels as much as possible to realize HRWS and GMTI by two channels along with two additional equivalent channels. The proposed method can break through the PRF restriction due to the range ambiguity resolving (low PRF required) and the Doppler spectrum ambiguity resolving (high PRF required). This condition enables HRWS imaging. The channels are also used for moving target detection and unambiguous motion parameter estimation.

Before the proposed methods are presented in detail, the signals of the four channels are converted to the Doppler domain by using fast Fourier transform (FFT) in azimuth. The Doppler domain representations can be given by [8]

$$
\begin{aligned}
s_1(\tau,f_a)&=\frac{\sigma_c}{\sqrt{K_{a1}}}\sin c\left(B_r\left(\tau-\frac{2R_n}{c}\right)\right)rect\left[\frac{f_a-f_{dc1}}{B_a}\right]\\
&\quad\cdot\exp(-j\varphi_1)\exp\left(j\frac{\pi(f_a-f_{dc1})^2}{K_{a1}}\right),
\end{aligned}
\tag{19}
$$

$$
\begin{aligned}
s_2(\tau,f_a)&=\frac{\sigma_c}{\sqrt{K_{a2}}}\sin c\left(B_r\left(\tau-\frac{2R_n}{c}\right)\right)rect\left[\frac{f_a-f_{dc2}}{B_a}\right]\\
&\quad\cdot\exp(-j\varphi_2)\exp\left(j\frac{\pi(f_a-f_{dc2})^2}{K_{a2}}\right)\\
&\quad\times\exp\left(-j\frac{2\pi(f_a-f_{dc2})d}{v}\right),
\end{aligned}
\tag{20}
$$

$$s_3(\tau, f_a) = \frac{\sigma_c}{\sqrt{K_{a1}}} \sin c\left(B_r\left(\tau - \frac{2R_n}{c}\right)\right) rect\left[\frac{f_a - f_{dc1}}{B_a}\right] \cdot \exp(-j\varphi_1) \exp\left(j\frac{\pi (f_a - f_{dc1})^2}{K_{a1}}\right) \times \exp\left(-j\frac{\pi (f_a - f_{dc1})\, d}{v}\right), \quad (21)$$

$$s_4(\tau, f_a) = \frac{\sigma_c}{\sqrt{K_{a2}}} \sin c\left(B_r\left(\tau - \frac{2R_n}{c}\right)\right) rect\left[\frac{f_a - f_{dc2}}{B_a}\right] \cdot \exp(-j\varphi_2) \exp\left(j\frac{\pi (f_a - f_{dc2})^2}{K_{a2}}\right) \times \exp\left(-j\frac{\pi (f_a - f_{dc2})\, d}{v}\right). \quad (22)$$

Notably, the Doppler spectrum bandwidths of the four channels are the same as B_a, which can be derived by

$$B_a = |K_{a1} T_{a1}| = \frac{2v^2 f_{c1}}{cR_n} \frac{L_a}{v} = \frac{2vf_{c1}}{c} \frac{L_a}{R_n} = \frac{2vf_{c1}}{c}\theta_{bw} = \frac{2vf_{c1}}{c} \frac{c}{f_{c1} D} = \frac{2v}{D}. \quad (23)$$

That is, the Doppler bandwidth is independent on the carrier frequency. In (23), L_a is the synthetic aperture length and θ_{bw} and D denote the beam width and the azimuth aperture of the antenna, respectively. By introducing (17)–(18) into (19)–(22) and correcting the amplitude due to K_{a1} (or K_{a2}), the following expressions can be obtained:

$$s_1(\tau, f_a) = \sigma_c \sin c\left(B_r\left(\tau - \frac{2R_n}{c}\right)\right) rect\left[\frac{f_a - f_{dc1}}{B_a}\right] \cdot \exp\left(-j\frac{4\pi R_n f_{c1}}{c}\right) \exp\left(j\frac{\pi c R_n f_a^2}{2v^2 f_{c1}}\right) \cdot \exp\left(j\frac{2\pi R_n v_{rel}^2 f_{c1}}{cv^2}\right) \exp\left(-j\frac{2\pi R_n v_{rel}}{v^2} f_a\right), \quad (24)$$

$$s_2(\tau, f_a) = \sigma_c \sin c\left(B_r\left(\tau - \frac{2R_n}{c}\right)\right) rect\left[\frac{f_a - f_{dc2}}{B_a}\right] \cdot \exp\left(-j\frac{4\pi R_n f_{c2}}{c}\right) \exp\left(j\frac{\pi c R_n f_a^2}{2v^2 f_{c2}}\right) \exp\left(j\frac{2\pi R_n v_{rel}^2 f_{c2}}{cv^2}\right) \cdot \exp\left(-j\frac{2\pi R_n v_{rel}}{v^2} f_a\right) \exp\left(-j2\pi \frac{2d}{v}\left(f_a - \frac{2v_{rel} f_{c2}}{c}\right)\right), \quad (25)$$

$$s_3(\tau, f_a) = \sigma_c \sin c\left(B_r\left(\tau - \frac{2R_n}{c}\right)\right) rect\left[\frac{f_a - f_{dc1}}{B_a}\right] \cdot \exp\left(-j\frac{4\pi R_n f_{c1}}{c}\right) \exp\left(j\frac{\pi c R_n f_a^2}{2v^2 f_{c1}}\right) \exp\left(j\frac{2\pi R_n v_{rel}^2 f_{c1}}{cv^2}\right) \cdot \exp\left(-j\frac{2\pi R_n v_{rel}}{v^2} f_a\right) \exp\left(-j2\pi \frac{d}{v}\left(f_a - \frac{2v_{rel} f_{c1}}{c}\right)\right), \quad (26)$$

TABLE 2. Channels for different applications.

	HRWS	GMTI	
		Unambiguous case	Ambiguous case
Channel 1	√	√	√
Channel 2	√	-	√
Channel 3	-	√	√
Channel 4	-	-	√

$$s_4(\tau, f_a) = \sigma_c \sin c\left(B_r\left(\tau - \frac{2R_n}{c}\right)\right) rect\left[\frac{f_a - f_{dc2}}{B_a}\right] \cdot \exp\left(-j\frac{4\pi R_n f_{c2}}{c}\right) \exp\left(j\frac{\pi c R_n f_a^2}{2v^2 f_{c2}}\right) \exp\left(j\frac{2\pi R_n v_{rel}^2 f_{c2}}{cv^2}\right) \cdot \exp\left(-j\frac{2\pi R_n v_{rel}}{v^2} f_a\right) \exp\left(-j2\pi \frac{d}{v}\left(f_a - \frac{2v_{rel} f_{c2}}{c}\right)\right), \quad (27)$$

We prelist the channels used to different applications in Table 2 to easily comprehend the concept of realizing HRWS and GMTI.

A. HRWS

As mentioned earlier, HRWS suffers from difficult designing of PRF due to the tradeoff between widely observed swath (low PRF for unambiguous range) and high azimuth resolution (high PRF for unambiguous Doppler spectrum). In this subsection, the HRWS imaging is presented in detail by utilizing channels 1 and 2. In [25], the range resolution is improved under cross-track channels, where different matched filters are used for phase compensation to obtain the same phase term for different channels. This concept is applied in along track channels to improve azimuth resolution.

In accordance with (24) and (25), the azimuth signal in the focused range gate of channels 1 and 2 can be rewritten as

$$s_1(f_a) = \sigma_c rect\left[\frac{f_a - f_{dc1}}{B_a}\right] \exp\left(-j\frac{4\pi R_n f_{c1}}{c}\right) \cdot \exp\left(j\frac{2\pi R_n v_{rel}^2 f_{c1}}{cv^2}\right) \cdot \exp\left(j\frac{\pi c R_n f_a^2}{2v^2 f_{c1}}\right) \times \exp\left(-j\frac{2\pi R_n v_{rel}}{v^2} f_a\right), \quad (28)$$

$$s_2(f_a) = \sigma_c rect\left[\frac{f_a - f_{dc2}}{B_a}\right] \exp\left(-j\frac{4\pi R_n f_{c2}}{c}\right) \cdot \exp\left(j\frac{2\pi R_n v_{rel}^2 f_{c2}}{cv^2}\right) \exp\left(j\frac{\pi c R_n f_a^2}{2v^2 f_{c2}}\right) \cdot \exp\left(-j\frac{2\pi R_n v_{rel}}{v^2} f_a\right) \exp\left(-j2\pi \frac{2d}{v}\left(f_a - \frac{2v_{rel} f_{c2}}{c}\right)\right), \quad (29)$$

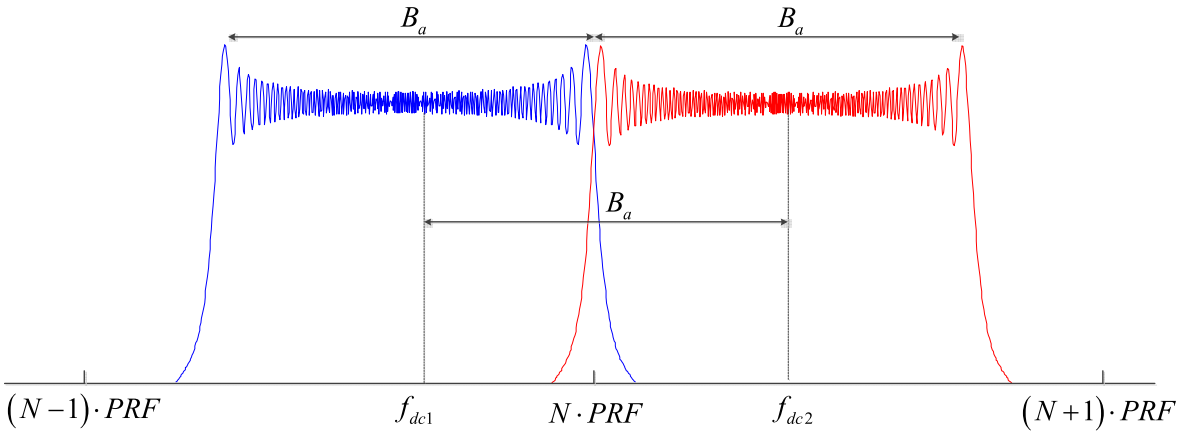

FIGURE 1. Conditions for Doppler band synthesis.

where the following constraint is supposed to keep the unambiguous Doppler spectrum:

$$B_a < PRF. \tag{30}$$

To compensate different phase terms, the matched function of channel 1 in the Doppler domain is designed as

$$s_{a1}(f_a) = rect\left[\frac{f_a - f_{dc1}}{B_a}\right]\exp\left(-j\frac{4\pi R_n f_{c1}}{c}\right) \cdot \exp\left(j\frac{2\pi R_n v_{rel}^2 f_{c1}}{cv^2}\right)\exp\left(j\frac{\pi c R_n f_a^2}{2v^2 f_{c1}}\right). \tag{31}$$

That of channel 2 is designed as

$$s_{a2}(f_a) = rect\left[\frac{f_a - f_{dc2}}{B_a}\right]\exp\left(-j\frac{4\pi R_n f_{c2}}{c}\right)\exp\left(j\frac{\pi c R_n f_a^2}{2v^2 f_{c2}}\right) \cdot \exp\left(j\frac{2\pi R_n v_{rel}^2 f_{c2}}{cv^2}\right)\exp\left(-j2\pi\frac{2d}{v}\left(f_a - \frac{2v_{rel}f_{c2}}{c}\right)\right), \tag{32}$$

where d and v_{rel} are pre-estimated, and the estimation methods are discussed in Section IV.

The matched results of channels 1 and 2 can be given by

$$s_1'(f_a) = s_1(f_a) * s_{a1}^*(f_a) = \sigma_c rect\left[\frac{f_a - f_{dc1}}{B_a}\right]\exp\left(-j\frac{2\pi R_n v_{rel}}{v^2}f_a\right), \tag{33}$$

$$s_2'(f_a) = s_2(f_a) * s_{a2}^*(f_a) = \sigma_c rect\left[\frac{f_a - f_{dc2}}{B_a}\right]\exp\left(-j\frac{2\pi R_n v_{rel}}{v^2}f_a\right), \tag{34}$$

where $(\cdot)^*$ denotes the conjugate transpose operation.

If the Doppler spectra of channels 1 and 2 are neighborhood, that is,

$$|f_{dc1} - f_{dc2}| = B_a, \tag{35}$$

then $s_1'(f_a)$ and $s_2'(f_a)$ can be processed coherently to synthesize a signal $s_{1+2}'(f_a)$ with the bandwidth of $2B_a$.

$$s_{1+2}'(f_a) = s_1'(f_a) + s_2'(f_a) = \sigma_c rect\left[\frac{f_a - (f_{dc1}+f_{dc2})/2}{2B_a}\right] \times \exp\left(-j\frac{2\pi R_n v_{rel}}{v^2}f_a\right). \tag{36}$$

We suppose that the following formula holds:

$$(f_{dc1}+f_{dc2})/2 = N\cdot PRF, \tag{37}$$

where N is an arbitrary integer, as shown in FIGURE 1. Thus, the condition of (37) is set to ensure that each Doppler spectrum is not split but complete; otherwise, the case shown in FIGURE 2 occurs, which brings poor split azimuth compression results.

Accordingly, (36) can be rewritten as

$$s_{1+2}'(f_a) = s_1'(f_a) + s_2'(f_a) = \sigma_c rect\left[\frac{f_a}{2B_a}\right]\exp\left(-j\frac{2\pi R_n v_{rel}}{v^2}f_a\right). \tag{38}$$

The inverse FFT is conducted in azimuth to complete the azimuth compression. Thus, the following azimuth compression results are obtained:

$$s'(\eta) = IFFT\left(s_{1+2}'(f_a)\right) = \sigma_c \sin c\left(2B_a\left(\eta - \frac{2\pi R_n v_{rel}}{v^2}\right)\right). \tag{39}$$

The azimuth resolution is improved twice because the original Doppler bandwidth B_a is doubled as $2B_a$ by combining the Doppler bands of different channels. However, the conventional azimuth compression results,

$$s_1'(\eta) = IFFT\left(s_1'(f_a)\right) = \sigma_c \sin c\left(B_a\left(\eta - \frac{2\pi R_n v_{rel}}{v^2}\right)\right), \tag{40}$$

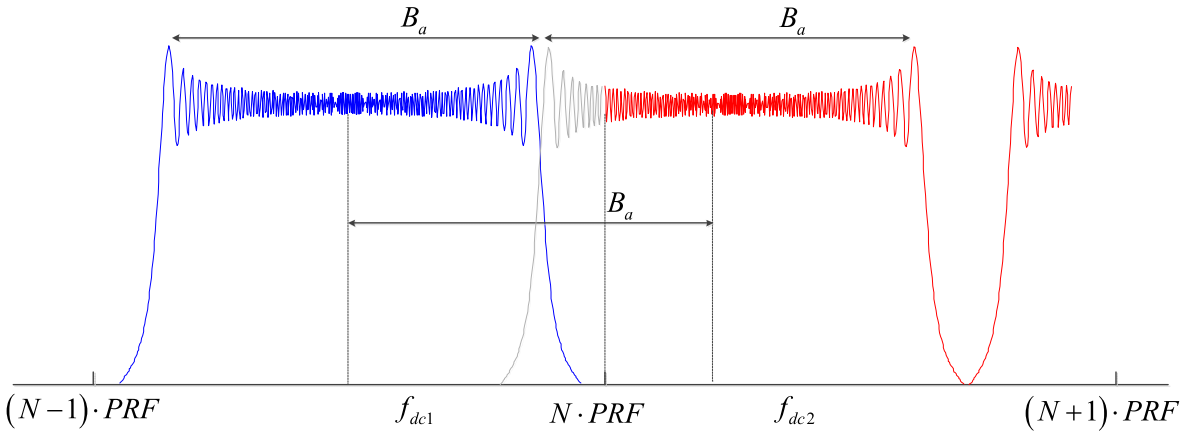

FIGURE 2. Case for unsatisfying the condition of (37).

$$s_2'(\eta) = IFFT\left(s_2'(f_a)\right) = \sigma_c \sin c\left(B_a\left(\eta - \frac{2\pi R_n v_{rel}}{v^2}\right)\right), \quad (41)$$

still possess low azimuth resolution.

As described in (35) and (37), the condition due to system parameters should be satisfied to guarantee the Doppler band synthesis, and the system parameter designing is analyzed in Section VI.

B. GMTI

The along track interferometry (ATI) method [1] is used to detect the moving target because the DPCA technology is limited by the PRF in the application [27]. The Doppler centroid caused by v_{rel} should be removed by the estimated v_{rel} to reduce its effect on moving target detection. The Doppler centroid correction technology is similar to the range walk correction [28]; thus, the detailed process is not presented in this paper.

After Doppler centroid due to v_{rel} is corrected, the range compression results of channels 1 and 3 can be written as follows for a moving target with radial velocity of v_r:

$$s_1(\tau,\eta) = \sigma_s \sin c\left(B_r\left(\tau - \frac{2R_n}{c}\right)\right) rect\left[\frac{\eta}{T_a}\right] \cdot \exp\left(-j\varphi_1 + j2\pi f_{dc1}'\eta - j\pi K_{a1}\eta^2\right), \quad (42)$$

$$s_3(\tau,\eta) = \sigma_s \sin c\left(B_r\left(\tau - \frac{2R_n}{c}\right)\right) rect\left[\frac{\eta}{T_a}\right] \cdot \exp\left(-j\varphi_1 + j2\pi f_{dc1}'\eta - j\pi K_{a1}\left(\eta - \frac{d}{2v}\right)^2\right), \quad (43)$$

where f_{dc1}' denotes the Doppler centroid corresponding to the moving target and can be given by

$$f_{dc1}' = \frac{2f_{c1}}{c} v_r. \quad (44)$$

In accordance with (24) and (26), the signals of the moving target can be transformed into the Doppler domain as

$$s_1(\tau,f_a) = \sigma_s \sin c\left(B_r\left(\tau - \frac{2R_n}{c}\right)\right) rect\left[\frac{f_a - f_{dc1}'}{B_a}\right] \cdot \exp\left(-j\frac{4\pi R_n f_{c1}}{c}\right) \exp\left(j\frac{2\pi R_n v_r^2 f_{c1}}{cv^2}\right) \cdot \exp\left(j\frac{\pi c R_n f_a^2}{2v^2 f_{c1}}\right) \exp\left(-j\frac{2\pi R_n v_r}{v^2} f_a\right), \quad (45)$$

$$s_3(\tau,f_a) = \sigma_s \sin c\left(B_r\left(\tau - \frac{2R_n}{c}\right)\right) rect\left[\frac{f_a - f_{dc1}'}{B_a}\right] \cdot \exp\left(-j\frac{4\pi R_n f_{c1}}{c}\right) \exp\left(j\frac{2\pi R_n v_r^2 f_{c1}}{cv^2}\right) \exp\left(j\frac{\pi c R_n f_a^2}{2v^2 f_{c1}}\right) \cdot \exp\left(-j\frac{2\pi R_n v_r}{v^2} f_a\right) \exp\left(-j2\pi \frac{d}{v}\left(f_a - \frac{2v_r f_{c1}}{c}\right)\right). \quad (46)$$

If the Doppler centroid and spectrum are not ambiguous, that is,

$$\left|f_{dc1}'\right| < PRF/2, \quad (47)$$

$$B_a < PRF, \quad (48)$$

then the conventional ATI, which uses channels 1 and 3, can be applied for moving target detection. In accordance with (45) and (46), the ATI result between channels 1 and 3 can be obtained by

$$s_{13}(\tau,f_a) = s_1^*(\tau,f_a) * \left[s_3(\tau,f_a)\cdot \exp\left(-j2\pi \frac{f_a d}{v}\right)\right] = (\sigma_s)^2 \sin c^2\left(B_r\left(\tau - \frac{2R_n}{c}\right)\right) \cdot rect\left[\frac{f_a - f_{dc1}'}{B_a}\right] \exp\left(j\frac{4\pi v_r f_{c1} d}{cv}\right). \quad (49)$$

The ATI phase $\Delta\varphi$ can be given by

$$\Delta\varphi = \frac{4\pi v_r f_{c1} d}{cv}. \tag{50}$$

The radial velocity is zero for stationary targets (or clutter). Thus, the ATI phase is also zero. By contrast, the nonzero radial velocity brings the nonzero ATI phase for moving targets. This condition is helpful for moving target detection. The phase or joint magnitude and phase [29] can be used for moving target detection, but the kernel of the methods includes the different interferometry phases between clutter and moving targets. Thus, the interferometry phase is mainly analyzed in this study.

The basic HRWS and GMTI methods have been presented so far. However, additional information should be provided. For HRWS imaging, some parameters (d and v_{rel}) and system parameters (PRF, f_{c1} and f_{c2}) need to be estimated and designed, respectively. For GMTI, the moving target detection under ambiguous case should be considered, and the motion parameters of the moving target should be estimated unambiguously. These analyses are addressed in Sections IV, V, and VI.

IV. UNAMBIGUOUS PARAMETER ESTIMATION

In this section, channel space and relative radial velocity (d and v_{rel}) are estimated first to accomplish HRWS imaging. Then, the motion parameter of the moving target is estimated for GMTI. The unambiguous estimations in contrast to the ambiguity case are also presented in this section.

A. CHANNEL SPACE AND RELATIVE RADIAL VELOCITY ESTIMATION

As mentioned earlier, the channel space and the relative radial velocity (d and v_{rel}) in (32) should be pre-estimated to compensate the different phase terms for Doppler band synthesis. The signals of channels 1 and 3 in the Doppler domain are used to estimate d and v_{rel}.

The interferometry between (24) and (26) is conducted to obtain the following interferometry results:

$$\begin{aligned} s_{13}(\tau, f_a) &= s_1^*(\tau, f_a) * s_3(\tau, f_a) \\ &= (\sigma_s)^2 \sin c^2\left(B_r\left(\tau - \frac{2R_n}{c}\right)\right) rect\left[\frac{f_a - f_{dc1}}{B_a}\right] \\ &\quad \cdot \exp\left(-j2\pi \frac{d}{v}\left(f_a - \frac{2v_{rel} f_{c1}}{c}\right)\right). \end{aligned} \tag{51}$$

The interferometry phase can be given by

$$\Delta\varphi(f_a) = -2\pi \frac{d}{v}\left(f_a - \frac{2v_{rel} f_{c1}}{c}\right). \tag{52}$$

Evidently, the interferometry phase $\Delta\varphi(f_a)$ is linearly trended over the Doppler frequency f_a. The slope k between the interferometry phase and the Doppler frequency f_a can be estimated. The channel space can also be estimated by [30]

$$\hat{d} = -kv/2\pi. \tag{53}$$

After the channel space is obtained, the relative radial velocity v_{rel} can be estimated by

$$\hat{v}_{rel} = \left(\frac{\Delta\varphi(f_a)\, v}{2\pi \hat{d}} + f_a\right)\frac{c}{2f_{c1}}, \tag{54}$$

where $\hat{v}_{rel}$ is supposed to be unambiguous. The ambiguous case is analyzed in the next subsection, together with the radial velocity estimation for moving targets.

The parameters are estimated by the phase that is wrapped around 2π. Thus, the estimations of (53) and (54) can be regarded as the ambiguity-free case. By contrast, the estimation under the ambiguity case is given together with the motion parameter estimation for moving targets in the next subsection.

B. UNAMBIGUOUS RADIAL VELOCITY ESTIMATION FOR MOVING TARGETS

The radial velocity v_r of the moving target can be estimated by the interferometry phase, that is,

$$\hat{v}_r = cv\Delta\varphi/4\pi f_{c1} d, \tag{55}$$

if the ATI phase $\Delta\varphi$ is unambiguous. The ATI phase is wrapped around 2π.

$$\Delta\varphi = \mathrm{mod}\left(\frac{4\pi v_r f_{c1} d}{cv}, 2\pi\right). \tag{56}$$

The maximum unambiguous radial velocity by the ATI phase can be calculated as

$$\hat{v}_{r,\max} = cv/4f_{c1} d. \tag{57}$$

When the radial velocity of the moving target is larger than $\hat{v}_{r,\max}$, the radial velocity estimation result is ambiguous, which should be avoided for the application of GMTI. However, the maximum unambiguous radial velocity is generally less than the interest radial velocities of moving targets. The parameters of Radarsat-2 [1] (TABLE 3) are used as examples, and the maximum unambiguous radial velocity can be calculated as $49.95 km/h$, which is too slow to unambiguously estimate the radial velocity of fast moving targets.

For the ambiguous case, two look data are constructed in the range frequency domain, and the interferometry between the two look data is used to resolve the ambiguity.

The range compression results of (42) and (43) are transformed into the range frequency f_r domain by FFT in range. Accordingly, the signal of the moving target in the Doppler domain can be written as

$$\begin{aligned} &s_1(f_r, f_a) \\ &= \sigma_s rect\left[\frac{f_r}{B_r}\right] rect\left[\frac{f_a - f'_{dc1}}{B_a}\right] \\ &\quad \cdot \exp\left(-j\frac{4\pi R_n (f_{c1} + f_r)}{c}\right) \exp\left(j\frac{\pi c R_n f_a^2}{2v^2 (f_{c1} + f_r)}\right) \\ &\quad \cdot \exp\left(j\frac{2\pi R_n v_r^2 (f_{c1} + f_r)}{cv^2}\right) \exp\left(-j\frac{2\pi R_n v_r}{v^2} f_a\right), \end{aligned} \tag{58}$$

TABLE 3. System parameters of Radarsat-2.

Parameters	symbols	values
Wavelength/m	λ	0.0555
Band width/MHz	B_r	50
Channel space/m	d	7.5
Orbital satellite velocity /(m/s)	v	7500
Pulse repetition frequency/Hz	PRF	1869
Nearest slant range/km	R_n	917.1

$$
\begin{aligned}
&s_3(f_r, f_a) \\
&= \sigma_s rect\left[\frac{f_r}{B_r}\right] rect\left[\frac{f_a - f'_{dc1}}{B_a}\right] \\
&\quad \cdot \exp\left(-j\frac{4\pi R_n (f_{c1}+f_r)}{c}\right) \exp\left(j\frac{\pi c R_n f_a^2}{2v^2 (f_{c1}+f_r)}\right) \\
&\quad \cdot \exp\left(j\frac{2\pi R_n v_r^2 (f_{c1}+f_r)}{cv^2}\right) \exp\left(-j\frac{2\pi R_n v_r}{v^2} f_a\right) \\
&\quad \cdot \exp\left(-j2\pi \frac{d}{v}\left(f_a - \frac{2v_r (f_{c1}+f_r)}{c}\right)\right),
\end{aligned} \tag{59}
$$

ATI is conducted in the (f_r, f_a) domain to obtain the following interferometry result:

$$
\begin{aligned}
s_{13}(f_r, f_a) &= s_1^*(f_r, f_a) * \left[s_3(f_r, f_a) \cdot \exp\left(-j2\pi \frac{f_a d}{v}\right)\right] \\
&= (\sigma_s)^2 rect\left[\frac{f_r}{B_r}\right] rect\left[\frac{f_a - f'_{dc1}}{B_a}\right] \\
&\quad \times \exp\left(j\frac{4\pi v_r (f_{c1}+f_r) d}{cv}\right).
\end{aligned} \tag{60}
$$

Two look data are constructed by the sub-band of the range frequency as

$$
\begin{aligned}
&s_{13}\left(f_r - \left(B_r/4\right), f_a\right) \\
&= (\sigma_s)^2 rect\left[\frac{f_r - \left(B_r/4\right)}{B_r/2}\right] \\
&\quad \cdot rect\left[\frac{f_a - f'_{dc1}}{B_a}\right] \exp\left(j\frac{4\pi v_r \left(f_{c1}+f_r - \left(B_r/4\right)\right) d}{cv}\right),
\end{aligned} \tag{61}
$$

$$
\begin{aligned}
&s_{13}\left(f_r - \left(-B_r/4\right), f_a\right) \\
&= (\sigma_s)^2 rect\left[\frac{f_r - \left(-B_r/4\right)}{B_r/2}\right] \\
&\quad \cdot rect\left[\frac{f_a - f'_{dc1}}{B_a}\right] \exp\left(j\frac{4\pi v_r \left(f_{c1}+f_r - \left(-B_r/4\right)\right) d}{cv}\right),
\end{aligned} \tag{62}
$$

By utilizing the following range frequency shift, the two look data can be rewritten as

$$
\begin{aligned}
s'_{13}(f_r, f_a) &= (\sigma_s)^2 rect\left[\frac{f_r}{B_r/2}\right] rect\left[\frac{f_a - f'_{dc1}}{B_a}\right] \\
&\quad \cdot \exp\left(j\frac{4\pi v_r \left(f_{c1}+f_r - \left(B_r/4\right)\right) d}{cv}\right),
\end{aligned} \tag{63}
$$

$$
\begin{aligned}
s''_{13}(f_r, f_a) &= (\sigma_s)^2 rect\left[\frac{f_r}{B_r/2}\right] rect\left[\frac{f_a - f'_{dc1}}{B_a}\right] \\
&\quad \cdot \exp\left(j\frac{4\pi v_r \left(f_{c1}+f_r - \left(-B_r/4\right)\right) d}{cv}\right),
\end{aligned} \tag{64}
$$

The interferometry between (63) and (64) is performed to obtain the following two look-data interferometry results:

$$
\begin{aligned}
\Delta s_{13}(f_r, f_a) &= s'^*_{13}(f_r, f_a) * s''_{13}(f_r, f_a) \\
&= (\sigma_s)^4 rect\left[\frac{f_r}{B_r/2}\right] rect\left[\frac{f_a - f'_{dc1}}{B_a}\right] \\
&\quad \times \exp\left(j\frac{4\pi v_r \left(B_r/2\right) d}{cv}\right).
\end{aligned} \tag{65}
$$

The corresponding interferometry phase is obtained as

$$
\begin{aligned}
\Delta\varphi' &= \frac{4\pi v_r \left(B_r/2\right) d}{cv} = \frac{4\pi v_r f_{c1} d}{cv} \frac{B_r}{2f_{c1}} \\
&= \Delta\varphi \cdot \frac{B_r}{2f_{c1}}.
\end{aligned} \tag{66}
$$

Then, the radial velocity can be estimated by

$$
\hat{v}'_r = \frac{cv\Delta\varphi'}{2\pi B_r d}. \tag{67}
$$

The bandwidth is considerably less than the carrier frequency, that is, $B_r \ll f_{c1}$. Thus, the unambiguous interferometry phase is improved by factor of $2f_{c1}/B_r$. As a result, the maximum unambiguous radial velocity of the moving targets is improved by $2f_{c1}/B_r$. The maximum unambiguous radial velocity can be calculated by the two look-data interferometry phase as

$$
\hat{v}'_{r,\max} = \frac{cv}{4f_{c1}d} \frac{2f_{c1}}{B_r} = \frac{cv}{2dB_r}. \tag{68}
$$

The maximum unambiguous radial velocity estimated by the two look-data interferometry phase can be calculated as $3000m/s$, with the improved factor of 216.2162, by substituting the system parameters of Radarsat-2 into (68) and $2f_{c1}/B_r$. The estimated maximum unambiguous radial velocity is considerably larger than the radial velocity of all the existing ground moving targets. This condition enables unambiguous radial velocity estimation for moving targets.

On the one hand, the two look-data interferometry method is beneficial for unambiguous estimation. On the other hand, this method decreases the interferometry phase and makes the phase insensitive to radial velocity. Although the estimated

maximum unambiguous radial velocity is improved, the interferometry phase becomes small even for fast ground moving targets. This condition brings difficulty for ATI method in detecting moving targets. Thus, the improved factor $2f_{c1}/B_r$ of the two look-data interferometry phase is designed too large to detect moving targets in noise and clutter background. The improved factor should be decreased to realize considerably robust moving target detection, which is presented in the next section.

V. ROBUST PERFORMANCE ANALYSIS

The robustness of the proposed methods is analyzed in this section, and the robust method is proposed to improve the performance.

A. ROBUST MOVING TARGET DETECTION AND UNAMBIGUOUS MOTION PARAMETER ESTIMATION METHOD

We propose the robust method to address the unsolved problem at the end of Section IV by considering the performance of moving target detection and unambiguous motion parameter estimation. The four channels are utilized to decrease the original improved factor $2f_{c1}/B_r$ of the two look-data interferometry method.

The interferometry between (45) and (46) is performed to obtain the following result:

$$\begin{aligned} s_{13}(\tau, f_a) &= s_1^*(\tau, f_a) * s_3(\tau, f_a) \\ &= (\sigma_s)^2 \sin c^2\left(B_r\left(\tau - \frac{2R_n}{c}\right)\right) rect\left[\frac{f_a - f'_{dc1}}{B_a}\right] \\ &\quad \cdot \exp\left(-j2\pi \frac{d}{v}\left(f_a - \frac{2v_r f_{c1}}{c}\right)\right). \end{aligned} \tag{69}$$

Similarly, the interferometry result between channels 2 and 4 in the Doppler domain can be expressed as

$$\begin{aligned} s_{24}(\tau, f_a) &= s_2^*(\tau, f_a) * s_4(\tau, f_a) \\ &= (\sigma_s)^2 \sin c^2\left(B_r\left(\tau - \frac{2R_n}{c}\right)\right) rect\left[\frac{f_a - f'_{dc2}}{B_a}\right] \\ &\quad \cdot \exp\left(-j2\pi \frac{d}{v}\left(f_a - \frac{2v_r f_{c2}}{c}\right)\right). \end{aligned} \tag{70}$$

Given azimuth sampling by PRF, the Doppler centroids of the moving target, namely, f'_{dc1} and f'_{dc2}, along with the Doppler spectrum, are located in the range of $[-PRF, PRF]$. For the unambiguous case, the ATI method can be used to detect the moving target, and the unambiguous Doppler centroid can be estimated by (44) and (55). However, for the ambiguous case, the estimated Doppler centroid is ambiguous provided the moving target can be detected. Nevertheless, the estimated ambiguous Doppler centroid can be used to shift the Doppler spectrum to zero Doppler centroid. That is, regardless of the existence or non-existence of Doppler centroid ambiguity, the estimated (unambiguous or ambiguous) Doppler centroids can be used to shift the Doppler spectrum of (69) and (70) into zero Doppler centroid as

$$\begin{aligned} s_{13}(\tau, f_a) &= (\sigma_s)^2 \sin c^2\left(B_r\left(\tau - \frac{2R_n}{c}\right)\right) \\ &\quad \cdot rect\left[\frac{f_a}{B_a}\right] \exp\left(-j2\pi \frac{d}{v}\left(f_a - \frac{2v_r f_{c1}}{c}\right)\right), \end{aligned} \tag{71}$$

$$\begin{aligned} s_{24}(\tau, f_a) &= (\sigma_s)^2 \sin c^2\left(B_r\left(\tau - \frac{2R_n}{c}\right)\right) \\ &\quad \cdot rect\left[\frac{f_a}{B_a}\right] \exp\left(-j2\pi \frac{d}{v}\left(f_a - \frac{2v_r f_{c2}}{c}\right)\right). \end{aligned} \tag{72}$$

The interferometry between (71) and (72) is performed to obtain the following interferometry results among four channels:

$$\begin{aligned} s_{1324}(\tau, f_a) &= s_{13}^*(\tau, f_a) * s_{24}(\tau, f_a) \\ &= (\sigma_s)^4 \sin c^4\left(B_r\left(\tau - \frac{2R_n}{c}\right)\right) \\ &\quad \cdot rect\left[\frac{f_a}{B_a}\right] \exp\left(j\frac{4\pi v_r d}{cv}(f_{c2} - f_{c1})\right). \end{aligned} \tag{73}$$

The corresponding interferometry phase can be given by

$$\begin{aligned} \Delta\varphi_{1324}(\tau, f_a) &= \frac{4\pi v_r d}{cv}(f_{c2} - f_{c1}) \\ &= \frac{4\pi v_r f_{c1} d}{cv}\frac{f_{c2} - f_{c1}}{f_{c1}} \end{aligned} \tag{74}$$

with the improved factor of $\left|f_{c1}/(f_{c1} - f_{c2})\right|$. The radial velocity can be estimated by

$$\hat{v}''_r = \frac{cv\Delta\varphi_{1324}}{4\pi (f_{c2} - f_{c1}) d}. \tag{75}$$

The estimated maximum unambiguous radial velocity is

$$\hat{v}''_{r,\max}\frac{cv}{4f_{c1}d}\left|\frac{f_{c1}}{f_{c1} - f_{c2}}\right| = \frac{cv}{4d\,|f_{c1} - f_{c2}|}. \tag{76}$$

If the carrier frequency f_{c2} is set to 3.9 GHz, then the maximum unambiguous radial velocity and the improved factor can be calculated as $49.8205 m/s = 179.3537 km/h$ and 3.8462. This condition enables the unambiguous estimation for nearly all of the ground moving targets. Given that the improved factor is decreased, the interferometry phase is considerably more sensitive to the radial velocity than the two look-data interferometry method. The moving target detection performance should be considerably more robust than the two look-data interferometry method theoretically, as demonstrated by the simulation in Section VII.

The performance of moving target detection is improved by the four-channel interferometry. The unambiguous radial velocity estimation performance is also not decreased but improved because of the considerably sensitive phase to radial velocity. In this section, the ambiguity is resolved by signal processing, and some new algorithm such as optimization methods [31]–[32] and deep learning [33]–[37] may get much better results, which would be studied in our future work.

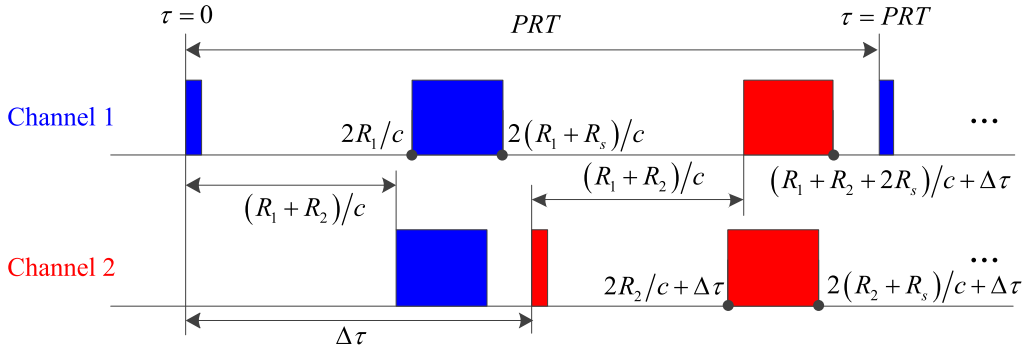

FIGURE 3. Timing diagrams of case 1.

B. EFFECT CAUSED BY THE AZIMUTH VELOCITY OF THE MOVING TARGET

In general, the moving target possesses not only radial velocity but also azimuth velocity. As mentioned earlier, the azimuth velocity of the moving target is not analyzed. In this subsection, the azimuth velocity is only added into the signal model of the moving target. The moving target detection is nearly independent on the azimuth velocity of the moving target. Accordingly, the effect on radial velocity estimation is mainly analyzed, and the solution is proposed to avoid affecting the radial velocity estimation.

When the azimuth velocity of the moving target v_a is analyzed, the signals of (71) and (72) can be rewritten as

$$\begin{aligned} &s'_{13}(\tau, f_a) \\ &= (\sigma_s)^2 \sin c^2\left(B_r\left(\tau - \frac{2R_n}{c}\right)\right) \\ &\quad \cdot rect\left[\frac{f_a}{B_a}\right] \exp\left(-j2\pi \frac{d}{v - v_a}\left(f_a - \frac{2v_r f_{c1}}{c}\right)\right), \end{aligned} \tag{77}$$

$$\begin{aligned} &s'_{24}(\tau, f_a) \\ &= (\sigma_s)^2 \sin c^2\left(B_r\left(\tau - \frac{2R_n}{c}\right)\right) \\ &\quad \cdot rect\left[\frac{f_a}{B_a}\right] \exp\left(-j2\pi \frac{d}{v - v_a}\left(f_a - \frac{2v_r f_{c2}}{c}\right)\right). \end{aligned} \tag{78}$$

The four-channel interferometry phase can be given as

$$\begin{aligned} \Delta\varphi'_{1324}(\tau, f_a) &= \frac{4\pi v_r d}{c(v - v_a)}(f_{c2} - f_{c1}) \\ &= \frac{4\pi v_r f_{c1} d}{c(v - v_a)} \frac{f_{c2} - f_{c1}}{f_{c1}}. \end{aligned} \tag{79}$$

The radial velocity can be estimated by

$$\hat{v}'''_r = \frac{c(v - v_a)\Delta\varphi'_{1324}}{4\pi(f_{c2} - f_{c1})d}. \tag{80}$$

Notably, the radial velocity estimation suffers from the unknown azimuth velocity, that is, the azimuth velocity should be pre-estimated prior to radial velocity estimation.

The interferometry result (77) or (78) in the Doppler domain is used to estimate the azimuth velocity v_a. Similar to the channel space estimation, the slope k' between the interferometry phase and the Doppler frequency is used for azimuth velocity estimation.

$$\hat{v}_a = \frac{2\pi d}{k'} + v, \tag{81}$$

where the channel space d is known or pre-estimated. For the case of unknown d along with ambiguity, the azimuth velocity can be estimated by utilizing the two look-data interferometry method.

VI. SYSTEM PARAMETER DESIGN

The proposed methods are used to realize HRWS imaging and GMTI. The ambiguity, which is a key problem of GMTI, is resolved by the two look-data or four-channel interferometry. However, for the HRWS imaging, some constraints, such as (30), (35), and (37), should be satisfied. In this section, we devote our efforts to satisfy these constraints by system parameter design.

For convenience, the constraints are rewritten in this section as

$$B_a < PRF, \tag{82}$$

$$|f_{dc1} - f_{dc2}| = B_a, \tag{83}$$

$$(f_{dc1} + f_{dc2})/2 = N \cdot PRF. \tag{84}$$

As mentioned earlier, the PRF is difficult to design. Thus, the system parameters containing PRF, Doppler bandwidth, and transmitted carrier frequencies should be designed properly to meet the requirements.

The requirements of the azimuth resolution and the observed range swath are determined. Our strategy involves the following steps. First, the PRF range is designed by the observed range swath. Then, the Doppler bandwidth is designed as wide as possible in the possible PRF range to obtain the highest azimuth resolution. Finally, the carrier frequencies are determined by (83) and (84).

A. PRF DESIGN

Given the observed range swath R_s and channel isolation (i.e., the channels transmit signals in different times), the PRF can be designed as in FIGURE 3 and 4. *PRT* denotes

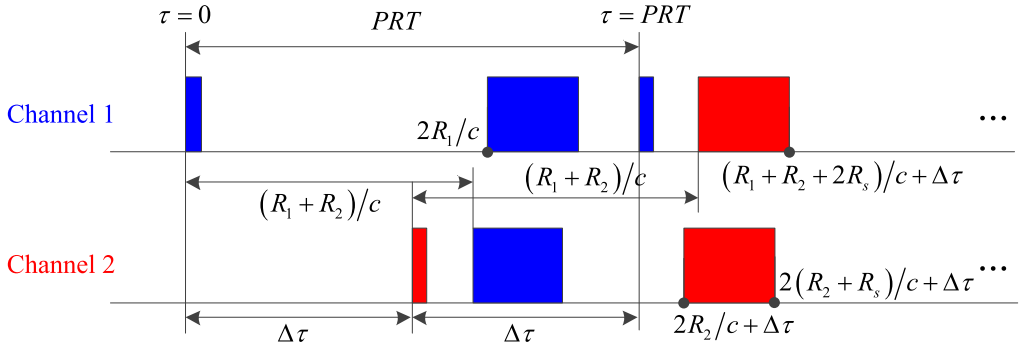

FIGURE 4. Timing diagrams of case 2.

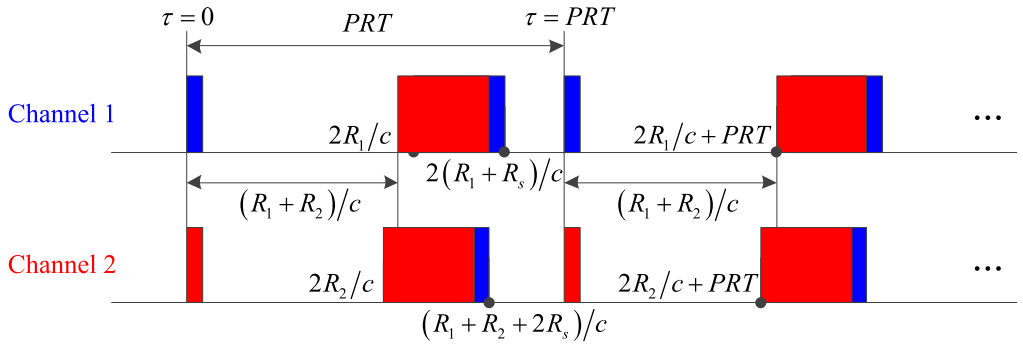

FIGURE 5. Timing diagrams of case 3.

the pulse repetition time, $\Delta\tau$ is the time interval of two transmitting channels, and $2\Delta\tau = PRT$ is held.

For case 1 in FIGURE 3, channel 1 transmits signals at $\Delta\tau = 0$. Moreover, channel 2 transmits signals after the echo of channel 1 has been received by both channels, i.e.,

$$\Delta\tau = \frac{PRT}{2} > \max\left\{\frac{2\,(R_1+R_s)}{c}, \frac{(R_1+R_2+2R_s)}{c}\right\}. \quad (85)$$

Similarly, the transmitting time of channel 1 should be determined by the echo of the transmitted signals of channel 2, that is,

$$PRT > \Delta\tau + \max\left\{\frac{2\,(R_2+R_s)}{c}, \frac{(R_1+R_2+2R_s)}{c}\right\}. \quad (86)$$

Substituting (85) into (86) yields the following PRF range corresponding to case 1:

$$PRT_1 > \max\left\{\frac{(3R_1+R_2+3R_s)}{c}, \frac{(R_1+3R_2+3R_s)}{c}\right\}. \quad (87)$$

For case 2 in FIGURE 4, channel 2 transmits signals before the echo of channel 1 arrives to both channels, that is,

$$\Delta\tau < \min\left\{\frac{2R_1}{c}, \frac{(R_1+R_2)}{c}\right\}. \quad (88)$$

Channel 1 transmits signals after the echo of channel 1 has been received by both channels, that is,

$$PRT > \max\left\{\frac{2\,(R_1+R_s)}{c}, \frac{(R_1+R_2+2R_s)}{c}\right\}. \quad (89)$$

Meanwhile, the transmitting time of channel 1 should not be overlapped with the received echoes by both channels corresponding to the transmitted signals by channel 2, i.e.,

$$PRT + T_r < \min\left\{\frac{(R_1+R_2)}{c}, \frac{2R_2}{c}\right\} + \Delta\tau. \quad (90)$$

Then, the PRF range for case 2 can be obtained by combining (88)–(90) as

$$\max\left\{\frac{2\,(R_1+R_s)}{c}, \frac{(R_1+R_2+2R_s)}{c}\right\} < PRT_2 < \min\left\{\frac{(3R_1+R_2)}{c}, \frac{(R_1+3R_2)}{c}\right\} - T_r. \quad (91)$$

In the analyses above (FIGURE 3 and 4), channel isolation is considered to obtain considerably low PRF. The signals with different carrier frequencies can be separated from each other in the range frequency domain. Thus, the isolation of channel level may be ignored by utilizing the isolation of signal level. The timing of transmitting and receiving by dual channels can be described as case 3 in FIGURE 5, in which both channels transmit signals at the same time.

Given that the transmitted signals do not overlap with the echoes, we should satisfy the following relationships:

$$PRT_3 > \max\left\{\frac{2\,(R_1+R_s)}{c}, \frac{(R_1+R_2+2R_s)}{c}\right\}, \quad (92)$$

$$T_r < \min\left\{\frac{(R_1+R_2)}{c}, \frac{2R_2}{c}\right\}, \quad (93)$$

where (93) can be satisfied in general.

Comparing (92) with (87) and (91) shows that FIGURE 5 provides the minimum PRT, whereas FIGURE 3 needs the maximum PRT. The maximum PRF can be achieved by FIGURE 5. Notably, all the timing diagrams in FIGURE 3–5 are designed by considering the same range swath. In summary, the PRF can be designed in the ranges of (87), (91), and (92) given the same range swath.

B. DOPPLER BANDWIDTH AND CARRIER FREQUENCY DESIGN

As mentioned earlier, different PRFs in the ranges of (87), (91), and (92) can be used to realize the same range swath. The PRF should be selected as high as possible to avoid the Doppler spectrum ambiguity for achieving high azimuth resolution. The sampling ratio by PRF in azimuth is designed as 1.1–1.4 to reduce the power of Doppler spectrum ambiguity [13]. Then, the Doppler bandwidth can be designed by

$$\frac{PRF}{1.4} < B_a < \frac{PRF}{1.1}. \tag{94}$$

For convenience, (94) can be rewritten as

$$\frac{1}{1.4} < \frac{B_a}{PRF} < \frac{1}{1.1} \Rightarrow 0.7143 < \frac{B_a}{PRF} < 0.9091. \tag{95}$$

After the PRF and Doppler bandwidth are determined, the carrier frequencies can be designed by (83) and (84). The isolation of signal level should also be considered for carrier frequency design. For example, the carrier frequencies are selected in different wave bands.

VII. SIMULATIONS AND ANALYSIS

In this section, simulations are conducted to demonstrate the effectiveness of the proposed methods. Simulation conditions are listed in TABLE 3, which keeps the same with that of Radarsat-2.

A. AZIMUTH RESOLUTION IMPROVING BY DOPPLER BAND SYNTHESIS

The Doppler spectra of channels 1 and 2 are shown in FIGURE 6.

FIGURE 6 shows that the Doppler frequency response of each channel is similar but different. The Doppler centroids are separated from each other, and the Doppler spectra of channels 1 and 2 are close to each other by considering the Doppler bandwidth. Then, the conditions hold for Doppler band synthesis.

By utilizing the Doppler band synthesizing technology, we achieve a doubled Doppler bandwidth, as shown in FIGURE 7. Notably, the doubled Doppler spectrum is successive and is thus useful for SAR imaging.

After azimuth compression, the normalized azimuth pulse response is as shown in FIGURE 8(a) and zoomed in FIGURE 8(b).

The figure shows that the azimuth resolution is improved twice using the Doppler band synthesizing technology. The azimuth compression results are similar to the range compression results in [25]. This similarity verifies the effectiveness

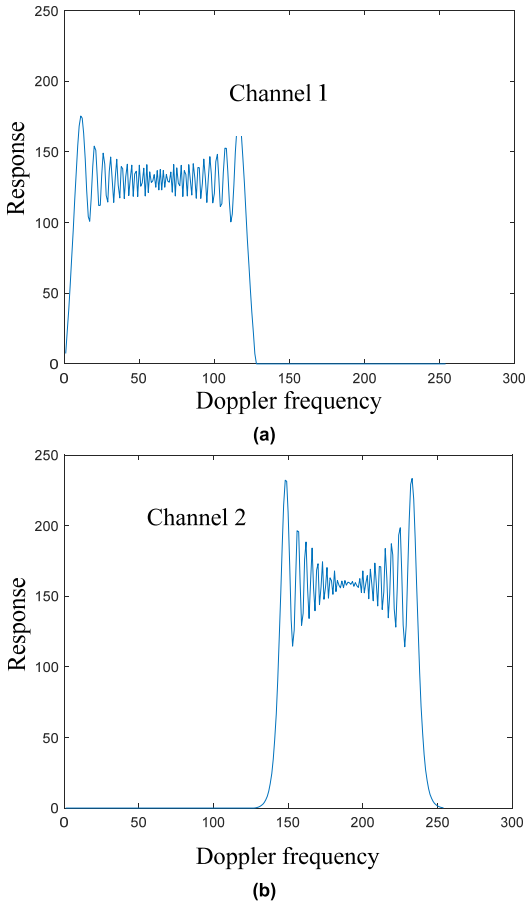

FIGURE 6. Doppler frequency response. (a)channel 1; (b) channel 2.

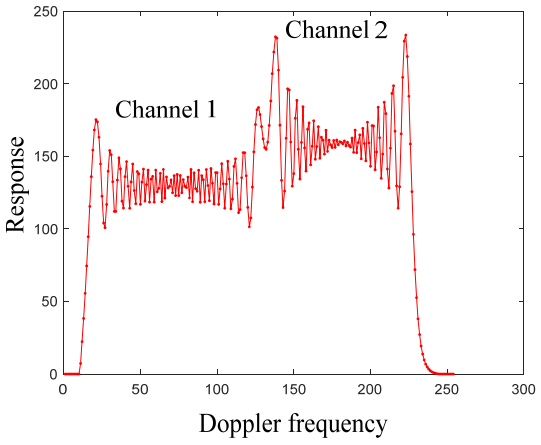

FIGURE 7. Doppler band synthesizing result.

of improving azimuth resolution by utilizing the Doppler band synthesizing technology. Moreover, the sidelobe of the azimuth compression results by using Doppler band synthesis is considerably lower than that without Doppler band synthesis. The sidelobe actually does not decrease but only becomes near the mainlobe because of the doubled Doppler bandwidth.

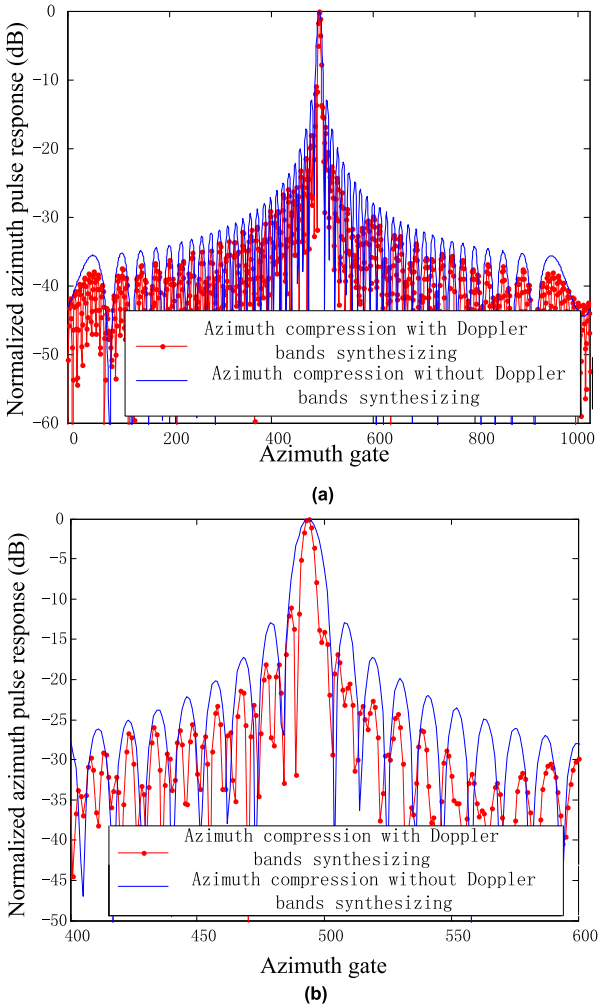

FIGURE 8. Normalized azimuth pulse response. (a) before zoomed results; (b) zoomed result.

B. GMTI PERFORMANCE SIMULATION AND ANALYSIS

The signal-to-noise ratio (SNR) loss is used to measure the effect of the ambiguity in quantization on moving target detection for analyzing the GMTI performance. The SNR loss, which is the peak power ratio between the zeroth ambiguous accumulated results and the unambiguous accumulated results, can be calculated by [8]

$$SNR_{loss} = 10\log_{10}\left(\left(B_0^2\left(B_a, PRF, f_{dc}^*\right)\cdot \bar{G}_0^2\right)\Big/\left(B_a^2\cdot \bar{G}_m^2\right)\right), \tag{96}$$

where $\bar{G}_0$ and $\bar{G}_m$ denote the average magnitudes of the two-way azimuth antenna pattern of the zeroth ambiguous target spectrum and the entire mainlobe target signal, respectively. The spectral width of the zeroth ambiguous target spectrum can be given by [8]

$$B_0\left(B_a, PRF, f_{dc}^*\right) = \min\left(B_a/2 + f_{dc}^*, PRF/2\right) - \max\left(-B_a/2 + f_{dc}^*, -PRF/2\right), \tag{97}$$

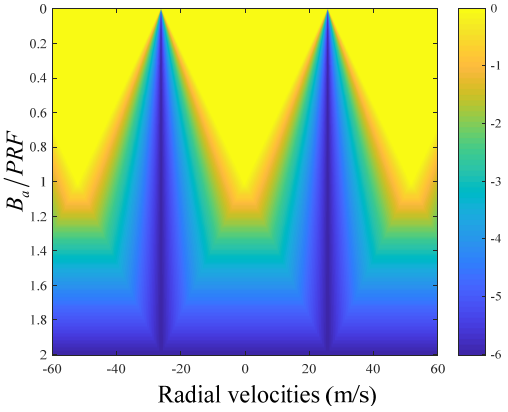

FIGURE 9. ATI-based SNR loss.

where f_{dc}^* denotes the Doppler centroid located in the range of $f_{dc}^* \in [-PRF, PRF]$ and can be calculated by its corresponding unambiguous Doppler centroid as

$$f_{dc}^* = \begin{cases} \text{mod}\left(f_{dc}, PRF\right) - PRF & if\ \text{mod}\left(f_{dc}, PRF\right) > PRF/2 \\ \text{mod}\left(f_{dc}, PRF\right) & otherwise, \end{cases} \tag{98}$$

where mod (x, y) denotes the modulus after x divided by y.

As mentioned earlier, the ATI-based Doppler centroid due to radial velocity can be expressed as

$$f_{dc} = \frac{2f_{c1}}{c}v_r. \tag{99}$$

The two look-data interferometry-based Doppler centroid can be given by

$$f'_{dc} = f_{dc}\frac{B_r}{2f_{c1}} = \frac{2f_{c1}}{c}\frac{B_r}{2f_{c1}}v_r = \frac{B_r}{c}v_r. \tag{100}$$

The four-channel interferometry-based Doppler centroid can be calculated by

$$f''_{dc} = f_{dc}\frac{|f_{c1} - f_{c2}|}{f_{c1}} = \frac{2f_{c1}}{c}\frac{|f_{c1} - f_{c2}|}{f_{c1}}v_r = \frac{2\,|f_{c1} - f_{c2}|}{c}v_r. \tag{101}$$

For ground moving targets, the radial velocity of interest is set as $v_r \in [-60m/s, 60m/s]$. Then, the SNR loss of different methods can be computed by (96)–(101). The simulated results are shown in FIGURE 9–11.

As mentioned earlier, the Doppler bandwidth range of $PRF/1.4 < B_a < PRF/1.1$ is mainly analyzed. FIGURE 9 shows that the SNR loss of the ATI method reaches the maximum of -6 dB when the radial velocity equals to the first blind velocity of $27.75m/s$ as in FIGURE 12. FIGURE 10 shows that the SNR of the two look-data interferometry method is not decreased in the range of interested radial velocities because the interferometry phase is greatly decreased by $2f_{c1}/B_r$. However, as mentioned above, the small two look-data interferometry phase (FIGURE 12)

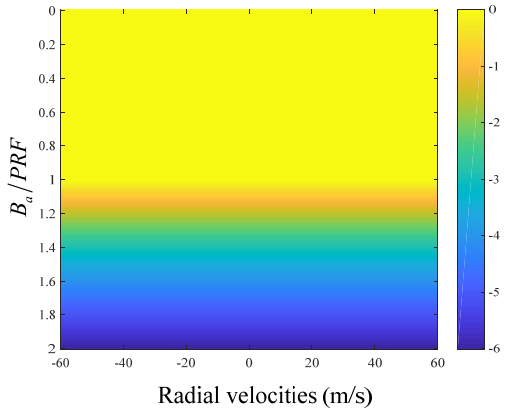

FIGURE 10. Two look-data interferometry-based SNR loss.

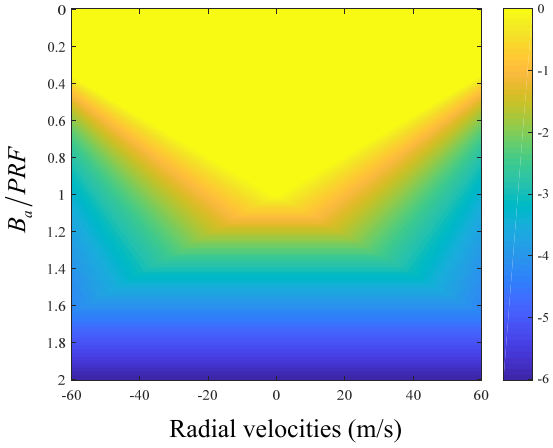

FIGURE 11. Four-channel interferometry-based SNR loss.

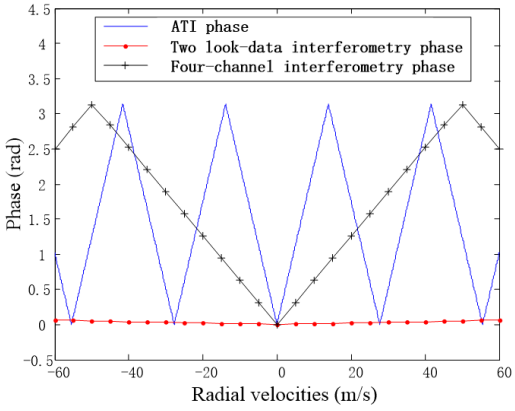

FIGURE 12. Interferometry phases.

causes difficulty in detecting moving targets, especially fast moving targets. Thus, the four-channel interferometry is proposed to reduce the improved factor from $2f_{c1}/B_r$ to $f_{c1}/|f_{c1}-f_{c2}|$. As shown in FIGURE 11 and 12, the SNR loss becomes worse than that by two look-data interferometry. Nevertheless, the phases corresponding to the interested

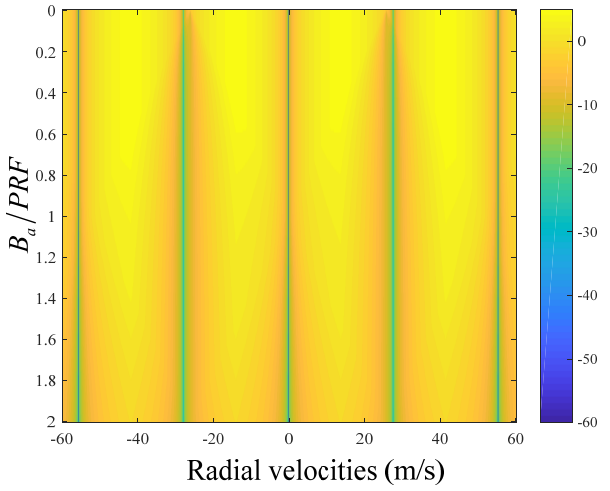

FIGURE 13. ATI-based SNR.

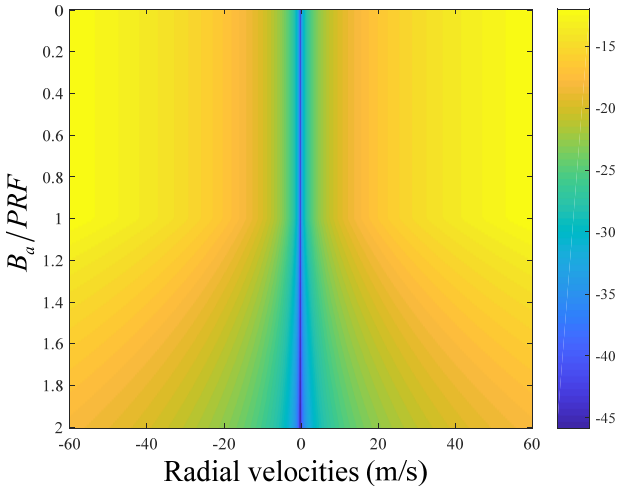

FIGURE 14. Two look-data interferometry-based SNR.

radial velocities are increased. This condition is evidently beneficial for moving target detection.

The SNR is also compared among three methods. The results are shown in FIGURE 13–16. The comparison curves in FIGURE 16 are obtained when B_a/PRF equals 0.8 due to (95). FIGURE 13 and 16 show that several blind velocities exist in the ATI method, and the SNR becomes zero theoretically when the radial velocity reaches the blind velocities. The radial velocities of the blind velocity areas shown in FIGURE 16 are close to the blind velocities. Thus, these areas may miss moving targets during detection due to their low SNR. FIGURE 14 and 15 show that the SNR results of the two look-data interferometry and four-channel interferometry methods are similar to each other. However, they differ in SNR, as shown FIGURE 16. The SNR of the proposed four-channel interferometry method is approximately 16.7370 dB higher than that of the two look-data interferometry method on average. Thus, the former method is evidently conducive to moving target detection because of the extra two channels

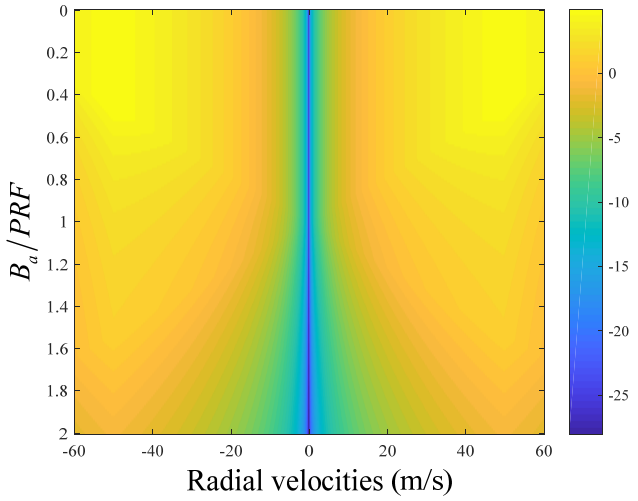

FIGURE 15. ATI-based SNR.

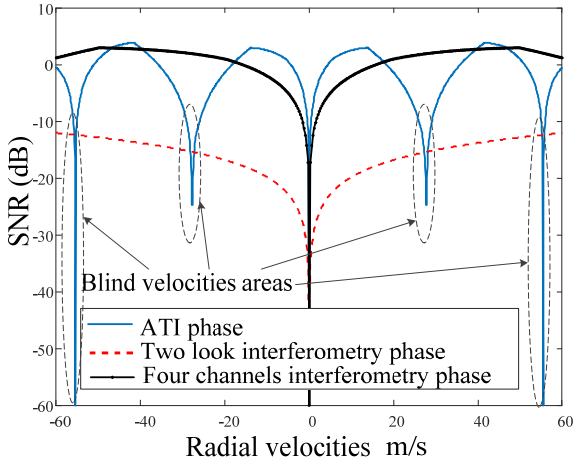

FIGURE 16. SNR comparison between the methods.

that introduce the SNR gain. No ambiguous and blind velocities exist in the range of $v_r \in [-60m/s, 60m/s]$. This condition is beneficial for moving target detection and velocity estimation.

VIII. CONCLUSION

We utilize the Doppler band synthesizing technology to double the Doppler bandwidth for improving the azimuth resolution to achieve HRWS imaging with low PRF in dual-channel SAR. This work can be used under the conditions that the condition of (37) holds, keeping each Doppler spectrum of each channel being not split but complete. Low PRF introduces ambiguity to moving targets. Thus, two look data are constructed in the range frequency domain, and the two look-data interferometry method is proposed to resolve the ambiguity. However, the ambiguity is resolved by decreasing the interferometry phase, which results in the insensitivity of this phase to the radial velocity of the moving targets. This condition is not helpful for moving target detection. We propose another interferometry among four channels (two real channels and two equivalent channels) to increase the interferometry phase for overcoming the aforementioned problems. The increased interferometry phase is unambiguous for the interested radial velocities of ground moving targets. Simulations verify the effectiveness of the proposed methods.

The contributions of this study are summarized as follows. We utilize the Doppler band synthesizing technology to achieve HRWS imaging with low PRF. Under this configuration, the HRWS SAR–GMTI is analyzed comprehensively. The analysis provides the theoretical basis for multichannel HRWS SAR–GMTI. As mentioned earlier, the interferometry phase is mainly analyzed as the kernel of the moving target detection methods. However, the analysis on the specific moving target detection methods require further investigation that focuses on multichannel HRWS SAR-based detection of ground moving targets. Moreover, some array signal processing methods [38]–[40] should be considered to improve the performance further.

REFERENCES

[1] C. H. Gierull, I. Sikaneta, and D. Cerutti-Maori, "Two-step detector for RADARSAT-2's experimental GMTI mode," *IEEE Trans. Geosci. Remote Sens.*, vol. 51, no. 1, pp. 436–454, Jan. 2013.

[2] Y. Zhang, W. Xiong, X. Dong, C. Hu, and Y. Sun, "GRFT-based moving ship target detection and imaging in geosynchronous SAR," *Remote Sens.*, vol. 10, no. 12, p. 2002, 2018.

[3] X. Zhang, Z. He, B. Liao, Y. Yang, J. Zhang, and X. Zhang, "Flexible array response control via oblique projection," *IEEE Trans. Signal Process.*, vol. 67, no. 12, pp. 3126–3139, Jun. 2019.

[4] L. Wan, G. Han, D. Zhang, A. Li, and N. Feng, "Distributed DOA estimation for arbitrary topology structure of mobile wireless sensor network using cognitive radio," *Wireless Pers. Commun.*, vol. 93, no. 2, pp. 431–445, Feb. 2017.

[5] C. Wen, C. Ma, J. Peng, and J. Wu, "Bistatic FDA-MIMO radar space-time adaptive processing," *Signal Process.*, vol. 163, no. 1, pp. 201–212, 2019.

[6] G. Li, X.-G. Xia, J. Xu, and Y.-N. Peng, "A velocity estimation algorithm of moving targets using single antenna SAR," *IEEE Trans. Aerosp. Electron. Syst.*, vol. 45, no. 3, pp. 1052–1062, Jul. 2009.

[7] I. Sikaneta, C. H. Gierull, and D. Cerutti-Maori, "Optimum signal processing for multichannel SAR: With application to high-resolution wide-swath imaging," *IEEE Trans. Geosci. Remote Sens.*, vol. 52, no. 10, pp. 6095–6109, Oct. 2014.

[8] Y. Shu, G. Liao, and Z. Yang, "Design considerations of PRF for optimizing GMTI performance in azimuth multichannel SAR systems with HRWS imaging capability," *IEEE Trans. Geosci. Remote Sens.*, vol. 52, no. 4, pp. 2048–2063, Apr. 2014.

[9] N. Gebert and G. Krieger, "Azimuth phase center adaptation on transmit for high-resolution wide-swath SAR imaging," *IEEE Geosci. Remote Sens. Lett.*, vol. 6, no. 4, pp. 782–786, Oct. 2009.

[10] J. Su, H. Tao, M. Tao, J. Xie, Y. Wang, and L. Wang, "Time-varying SAR interference suppression based on delay-Doppler iterative decomposition algorithm," *Remote Sens.*, vol. 10, no. 9, p. 1491, 2018.

[11] D. Cerutti-Maori, I. Sikaneta, and C. H. Gierull, "Optimum SAR/GMTI processing and its application to the radar satellite RADARSAT-2 for traffic monitoring," *IEEE Trans. Geosci. Remote Sens.*, vol. 50, no. 10, pp. 3868–3881, Oct. 2012.

[12] C. H. Gierull and I. C. Sikaneta, "Estimating the effective number of looks in interferometric SAR data," *IEEE Trans. Geosci. Remote Sens.*, vol. 40, no. 8, pp. 1733–1742, Aug. 2002.

[13] I. G. Cumming and F. H. Wong, *Digital Processing of Synthetic Aperture Radar Data: Algorithms and Implementation*. Norwood, MA, USA: Artech House, 2005.

[14] F. Wen, J. Shi, and Z. Zhang, "Direction finding for bistatic MIMO radar with unknown spatially colored noise," *Circuits, Syst., Signal Process.*, pp. 1–13, Oct. 2019, doi: 10.1007/s00034-019-01260-5.

[15] F. Wen, C. Mao, and G. Zhang, "Direction finding in MIMO radar with large antenna arrays and nonorthogonal waveforms," *Digital Signal Process.*, vol. 94, pp. 75–83, Nov. 2019.
[16] F. Wen, Z. Zhang, and G. Zhang, "Joint DOD and DOA estimation for bistatic MIMO radar: A covariance trilinear decomposition perspective," *IEEE Access*, vol. 7, pp. 53273–53283, 2019.
[17] H. Huang, J. Yang, H. Huang, Y. Song, and G. Gui, "Deep learning for super-resolution channel estimation and doa estimation based massive MIMO system," *IEEE Trans. Veh. Technol.*, vol. 67, no. 9, pp. 8549–8560, Sep. 2018.
[18] F. Wen, Z. Zhang, K. Wang, G. Sheng, and G. Zhang, "Angle estimation and mutual coupling self-calibration for ULA-based bistatic MIMO radar," *Signal Process.*, vol. 144, pp. 61–67, Mar. 2018.
[19] F. Wen, X. Xiong, and Z. Zhang, "Angle and mutual coupling estimation in bistatic MIMO radar based on PARAFAC decomposition," *Digit. Signal Process.*, vol. 65, pp. 1–10, Jun. 2017.
[20] F. Wen, Z. Zhang, G. Zhang, Y. Zhang, X. Wang, and X. Zhang, "A tensor-based covariance differencing method for direction estimation in bistatic MIMO radar with unknown spatial colored noise," *IEEE Access*, vol. 5, pp. 18451–18458, 2017.
[21] C. Yang, Z. Lu, and Z. Yang, "Robust optimal sensor placement for uncertain structures with interval parameters," *IEEE Sensors J.*, vol. 18, no. 5, pp. 2031–2041, Mar. 2018.
[22] X. Zhang, Z. He, B. Liao, X. Zhang, and W. Peng, "Pattern synthesis for arbitrary arrays via weight vector orthogonal decomposition," *IEEE Trans. Signal Process.*, vol. 66, no. 5, pp. 1286–1299, Mar. 2018.
[23] C. Wen, J. X. Wu, Y. Zhou, and J. Peng, "Enhanced three-dimensional joint domain localized STAP for airborne FDA-MIMO radar under dense false-target jamming scenario," *IEEE Sensors J.*, vol. 13, no. 10, pp. 4154–4166, May 2018.
[24] C. Yang, K. Liang, X. Zhang, and X. Geng, "Sensor placement algorithm for structural health monitoring with redundancy elimination model based on sub-clustering strategy," *Mech. Syst. Signal Process.*, vol. 124, pp. 369–387, Jun. 2019.
[25] D. Cristallini, D. Pastina, and P. Lombardo, "Exploiting MIMO SAR potentialities with efficient cross-track constellation configurations for improved range resolution," *IEEE Trans. Geosci. Remote Sens.*, vol. 49, no. 1, pp. 38–52, Jan. 2011.
[26] Y.-C. Li, L. Zhang, B.-C. Liu, Y.-H. Quan, M.-D. Xing, and Z. Bao, "Stepped-frequency inverse synthetic aperture radar imaging based on adjacent pulse correlation integration and coherent processing," *IET Signal Process.*, vol. 5, no. 7, pp. 632–642, Oct. 2011.
[27] D. Cerutti-Maori and I. Sikaneta, "A generalization of DPCA processing for multichannel SAR/GMTI radars," *IEEE Trans. Geosci. Remote Sens.*, vol. 51, no. 1, pp. 560–572, Jan. 2013.
[28] J. Yang, C. Liu, and Y. Wang, "Imaging and parameter estimation of fast-moving targets with single-antenna SAR," *IEEE Geosci. Remote Sens. Lett.*, vol. 11, no. 2, pp. 529–533, Feb. 2014.
[29] G. Gao and G. T. Shi, "The CFAR detection of ground moving targets based on a joint metric of SAR interferogram's magnitude and phase," *IEEE Trans. Geosci. Remote Sens.*, vol. 50, no. 9, pp. 3618–3624, Sep. 2012.
[30] B. Liu, T. Wang, Y. Li, F. Shen, and Z. Bao, "Effects of Doppler aliasing on baseline estimation in multichannel SAR-GMTI and solutions to address these effects," *IEEE Trans. Geosci. Remote Sens.*, vol. 52, no. 10, pp. 6471–6487, Oct. 2014.
[31] X. Zhang, Z. He, X. Xia, B. Liao, X. Zhang, and Y. Yang, "OPARC: Optimal and precise array response control algorithm—Part I: Fundamentals," *IEEE Trans. Signal Process.*, vol. 67, no. 3, pp. 652–667, Feb. 2019.
[32] X. Zhang, Z. He, X.-G. Xia, B. Liao, X. Zhang, and Y. Yang, "OPARC: Optimal and precise array response control algorithm—Part II: Multi-points and applications," *IEEE Trans. Signal Process.*, vol. 67, no. 3, pp. 668–683, Feb. 2019.
[33] G. Gui, H. Sari, and E. Biglieri, "A new definition of fairness for non-orthogonal multiple access," *IEEE Commun. Lett.*, vol. 23, no. 7, pp. 1267–1271, May 2019.
[34] J. Wang, Y. Ding, S. Bian, Y. Peng, M. Liu, and G. Gui, "UL-CSI data driven deep learning for predicting DL-CSI in cellular FDD systems," *IEEE Access*, vol. 7, pp. 96105–96112, 2019.
[35] L. Wan, L. Sun, X. Kong, Y. Yuan, K. Sun, and F. Xia, "Task-driven resource assignment in mobile-edge computing exploiting evolutionary computation," *IEEE Wireless Commun.*, to be published, doi: 10.1109/MWC.001.1800582.
[36] Y. Wang, M. Liu, J. Yang, and G. Gui, "Data-driven deep learning for automatic modulation recognition in cognitive radios," *IEEE Trans. Veh. Technol.*, vol. 68, no. 4, pp. 4074–4077, Apr. 2019.
[37] G. Gui, H. Huang, Y. Song, and H. Sari, "Deep learning for an effective nonorthogonal multiple access scheme," *IEEE Trans. Veh. Technol.*, vol. 67, no. 9, pp. 8440–8450, Sep. 2018.
[38] H. Wang, L. Wan, M. Dong, K. Ota, and X. Wang, "Assistant vehicle localization based on three collaborative base stations via SBL-based robust DOA estimation," *IEEE Internet Things J.*, vol. 6, no. 3, pp. 5766–5777, Jun. 2019.
[39] X. Wang, L. Wan, M. Huang, C. Shen, and K. Zhang, "Polarization channel estimation for circular and non-circular signals in massive MIMO systems," *IEEE J. Sel. Topics Signal Process.*, vol. 13, no. 5, pp. 1001–1016, Sep. 2019.
[40] L. Wan, X. Kong, and F. Xia, "Joint range-Doppler-angle estimation for intelligent tracking of moving aerial targets," *IEEE Internet Things J.*, vol. 5, no. 3, pp. 1625–1636, Jun. 2018.

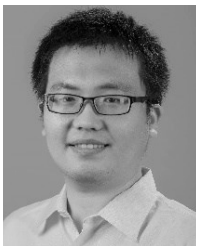

XUEPAN ZHANG was born in Hebei, China. He received the B.S. and Ph.D. degrees in electrical engineering from the National Laboratory of Radar Signal Processing, Xidian University, Xi'an, China, in 2010 and 2015, respectively. He is currently a Principal Investigator with the Qian Xuesen Laboratory of Space Technology, Beijing, China. His current research interests include synthetic aperture radar, ground moving target indication, and deep learning.

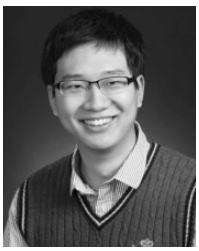

CHEN YANG received the bachelor's, master's, and Ph.D. degrees in engineering mechanics and solid mechanics from Beihang University (BUAA), Beijing, China, in 2010, 2013 and 2018, respectively.

He is currently an Associate Professor with the Qian Xuesen Laboratory of Space Technology, China Academy of Space Technology. He published over forty research articles in the journals, particularly in the area of intelligent optimization algorithms and its applications. His research interests include optimization theory, structural health monitoring, optimal sensor placement, structural dynamics, and thermal control.

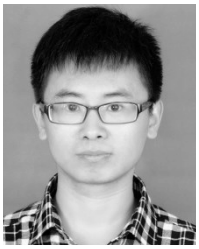

XUEJING ZHANG (S'17) was born in Hebei, China. He received the B.S. degree in electrical engineering from Huaqiao University, Xiamen, China, and the M.S. degree in signal and information processing from Xidian University, Xi'an, China, in 2011 and 2014, respectively. He is currently pursuing the Ph.D. degree in signal and information processing with the School of Information and Communication Engineering, University of Electronic Science and Technology of China (UESTC), Chengdu, China. Since November 2017, he has been a Visiting Student with the University of Delaware, Newark, DE, USA. His research interests include array signal processing and wireless communications.

QINGQING LIN was born in 1987. She received the B.S. and Ph.D. degrees in information and communication engineering from Harbin Engineering University, Harbin, China, in 2009 and 2013, respectively.

Since 2013, she has been a Research Assistant with the Qian Xuesen Laboratory of Space Technology, China Academy of Space Technology, Beijing, China. Her research interests include array signal processing and wireless sensor networks.